Article

Diagnostics on Power Electronics Converters by Means of Autoregressive Modelling

Roberto Diversi [1], Leonardo Sandrolini [1,*], Mattia Simonazzi [1], Nicolò Speciale [1] and Andrea Mariscotti [2]

1 Department of Electrical, Electronic, and Information Engineering (DEI), University of Bologna, 40136 Bologna, Italy; roberto.diversi@unibo.it (R.D.); mattia.simonazzi2@unibo.it (M.S.); nicolo.speciale@unibo.it (N.S.)
2 Department of Electrical, Electronics and Telecommunication Engineering and Naval Architecture (DITEN), University of Genova, 16145 Genova, Italy; andrea.mariscotti@unige.it
* Correspondence: leonardo.sandrolini@unibo.it

Abstract: Power conversion systems for wireless power transfer (WPT) applications have demanding requirements for continuity of service, besides being operated with stressing environmental conditions. Diagnostic and prognostic programs are thus quite useful and this work shows a novel approach based on the analysis of spectra of an autoregressive (AR) model to recognize a wide range of faulty devices, including incipient faults, when deviations from nominal parameters begin to manifest. AR modeling provides cleaner and easier to interpret spectra, where only the salient features remain, and they are more sensitive to variations in the corresponding time domain waveforms. A log spectral distance is calculated that successfully separates healthy and faulty states of the feeding single-phase inverter, even in challenging scenarios of poor signal-to-noise ratio.

Keywords: electromagnetic compatibility; conducted emissions; diagnostics; autoregressive model; data-driven techniques; SMPS; wireless power transfer

1. Introduction

Compared to AC grids, DC grids (and microgrids in particular) have higher reliability [1–3], lower power losses with better greater efficiency [4,5], and better power quality (PQ) with lower distortion levels (although the extensive use of static power conversion devices has raised the concern of an increasing supraharmonic pollution [6–8]). They also provide uninterruptible power supply characteristics [9,10], which are particularly useful for the continuity of service in specific applications and in general for mission critical systems.

The architecture of a DC grid consists of a distributed DC link that powers multiple loads through switching power converters. Therefore, both conducted emissions (CEs) and high-frequency converter impedance must be kept under control to maintain PQ and network stability, and ensure satisfactory operation of all connected devices. Such distributed architecture is particularly useful when putting together several pulsed loads with significant dynamics, as a quick power transfer is available by means of capacitive storage. An example of this scenario is a pool of power converters (inverters) feeding a wireless power transfer (WPT) system, charging electric vehicles while moving [11,12].

Another important aspect of static power converters is their availability, providing the above mentioned uninterrupted supply as part of modern grids with high system availability targets and levels of resiliency, in case of the use of redundant and oversized architectures. Other cases where static power converters' availability is significant are power drives with critical functions (e.g., emergency pumping or extraction of fumes) or being part of expensive industrial processes (e.g., high-performance tooling and machining, series production, etc.).

The improvement of availability and the prevention of long down times are strongly related to the implementation of effective and comprehensive diagnostics [13].

In general, CEs depend on the converter topology, load, and operating conditions, but also may change under variable supply conditions [14,15], temperature variations [15], and different cable lengths [16]. As a general control measure, EMI filters and spread spectrum techniques can reduce CEs, maximizing series inductance while minimizing at the same time shunt capacitance to ground, which can cause the flow of supraharmonic currents [17–19]. In our scenario, the DC bus capacitor at the inverter input acts as the first stage of filtering. The ripple on the input current, and thus the CEs towards the network, usually oscillates at twice the output current fundamental frequency, tuned at the WPT resonance frequency. The capacitor filters this lower frequency component, also attenuating higher frequency switching components.

For a converter supplying a resonant WPT system, the fundamental frequency of the output voltage and current equals the switching frequency. These systems use resonant compensation networks as band-pass filters, allowing square-wave operation with reduced harmonics. This produces a nearly sinusoidal input current at the network tuning frequency, regardless of the square driving voltage. The switching frequency is limited to a minimum, which equals the compensation network resonant frequency, thus reducing switching losses and avoiding complex control strategies [20]. Most analyses use a first harmonic approximation, enabling simplified equivalent circuit modeling using quantities at the fundamental frequency only. This simplifies analysis and design. The input current becomes a pulsed sinusoidal waveform with a fundamental at twice the switching frequency and only even harmonics appear.

However, failures or degradation in any of the converter components cause deviations from the theoretical waveforms [21]. Such failures or degradation and the consequential deterioration or deviation of the signals waveform have an impact on various aspects of the converter itself and of the WPT system in general. A loss of tuning translates into a reduced efficiency; that is relevant not only in an economical perspective, but also as a cause of temperature increase due to the increased losses. Operating at a higher temperature may reduce the useful life of the components and of the system; similarly, with waveforms that deviate from the nominal ones, components may experience excessive current or over-voltages, both impacting their durability.

A significant percentage of the component faults is represented by failures of the power electronic switches [22], which can occur for a number of reasons, such as chip-related (intrinsic) failures and package-related (extrinsic) failures. The former are mostly related to electrical over-stress (i.e., various forms of high current and high voltage stress), whereas the latter are commonly induced by thermo-mechanical over-stress [23–25]. In general, power electronic switch faults are classified as short- and open-circuit faults, with the latter being more difficult to detect in time [6,26–29].

Not addressing faults quickly can exacerbate problems, give rise to risks for the safe use and operation of the equipment, and increase maintenance costs. However, diagnosing faults is a lengthy process due to the complexity of power electronic systems, which contain many components. With power electronics becoming more complex and larger in scale, the need for effective fault diagnosis (FD) is becoming more and more vital [30].

Historically, inverter FD has developed along two principal methodologies: approaches founded on mathematical models [31–33] and data-driven techniques [6,30,34]. The former analyze the dynamics and properties of a system to forecast its expected behavior in both fault and normal scenarios. When an anomaly from the norm is found, it may be a sign that there is a problem. Despite excellent FD and detection precision, the model-based approach is challenging to implement due to the complexity of establishing a mathematical model of the fault. On the other hand, data-driven FD techniques rely on examining data gathered from the system. Data-driven techniques are used to extract patterns and relationships directly from the data, rather than explicitly modelling the behavior of the system. These techniques work by using historical data with both normal and defective

operation scenarios to train algorithms to find deviations or anomalies that point to the existence of a fault. Data-driven approaches are appropriate for complex systems with fluctuating operating conditions because they are more flexible with respect to different fault scenarios and do not necessitate extensive system modelling.

What we have collected in the mathematical model group, in [13], are further distinguished as "signal-based methods" and "model-based methods": the difference is subtle in that the former consider local signals at low level (hardware level) with minimal processing and fast response times (as it may be for the protection circuits of MOSFETS and IGBTs), whereas the latter develop a more complex algorithm, based on some kind of modeling of the normal and exceptional (or faulty) behavior of the converter. The proposed method acquires high-level signals (accessible at the terminals of the converter, rather than at its internal semiconductors and components) and evaluates them by applying a spectrum synthesizing approach based on auto-regressive (AR) models.

This paper analyzes the effects of faults in the switches of an H-bridge inverter feeding both a resistive load and a series–series compensated WPT system by means of autoregressive modelling. Autoregressive models are one of the most widely used tools for analyzing time series data and estimating spectra [35,36]. Their popularity stems from several key factors: there are simple and robust algorithms available for identifying AR models, online estimation methods are easy to implement, and AR models can provide more accurate spectral estimates than classical Fourier-based techniques [36,37]. These features make AR models a very interesting tool for FD systems [38–44], and also useful in the in the framework of edge-computing condition monitoring [45,46]. The use of AR models in FD consists of two main steps:

1. estimate an AR model of the measured signal $y(t)$ (vibration, current, etc.);
2. extract suitable features from the estimated model (prediction error variance, model coefficients, spectral density, etc.) that allow healthy conditions to be discriminated from faulty ones.

This is a black-box approach, which does not require any physical knowledge about the system to be diagnosed; for this reason it belongs to the so called data-driven FD methods [47–49].

The main original contribution of the work consists of demonstrating that it is possible to exploit the variation that the PSD of the AR model of the acquired signal undergoes in the presence of typical malfunctions compared to the healthy case. Both the ability to monitor the operating conditions of the system in real time and the ability to perform fault identification without notable tuning complexities are fundamental prerequisites for assessing the reliability of power electronic converters.

The paper is structured as follows. Section 2 describes the circuit topology, the electrical ruling equations and the relevant electrical parameters. Section 3 provides insight into the foundations of AR analysis and its application to FD. Results are then reported in Section 4, which is a long section where both the simpler circuit with resistive load and the more complete application including the WPT circuit are considered, for both significant failures in extreme electrical conditions and incipient faults. The discussion of the findings is included in the same section, whereas Section 5 summarizes the outcome of the work, its effectiveness, and its applicability.

2. System Characteristics

The considered power converter is an H-bridge inverter with GaN MOSFETs as switches. The equivalent circuit of the considered system is shown in Figure 1 for a generic resistive load and in Figure 2 considering the complete WPT system.

Very high switching frequencies (up to 300 kHz) can then be reached, compared to converters using traditional semiconductors. Indeed, GaN MOSFETs have high blocking voltage and good operating temperature while still enabling fast switching. Specifically, EPC2001C eGaN FETs are used, which have a drain-source on-resistance around 8 mΩ at

25 °C and 17.5 mΩ at 150 °C, measured at $V_{GS} = 6$ V and $I_{DS} = 27$ A. The required dead time (delay between gate signals representing a guard time) for these MOSFETs is 350 ns.
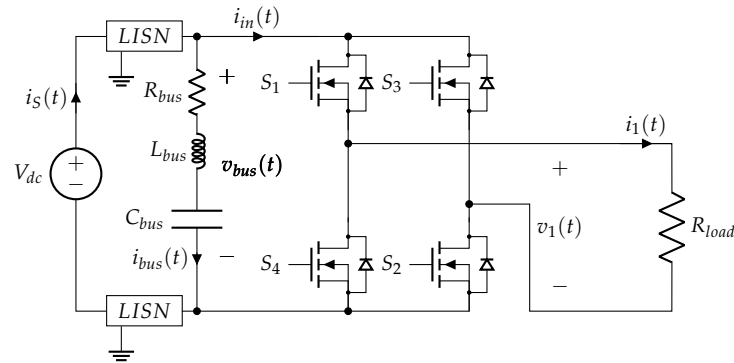

Figure 1. Equivalent circuit of the inverter feeding a resistive load.
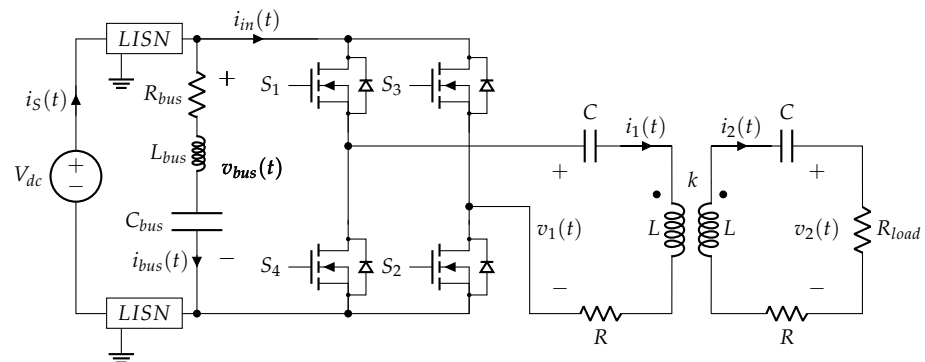

Figure 2. Equivalent circuit of the inverter feeding a WPT system.

The first filtering stage of the inverter input current is the DC bus capacitor bank, which ideally allows the DC component of the bridge current to flow in the DC power source. However, due to the parasitics, the capacitor does not behave ideally and its filtering characteristics should be properly considered. In general, a series R-L-C circuit is adequate to model the DC bus capacitor bank [50], whose parameters can be estimated through measurements and knowing the inverter schematic. In this case, the DC bus of the inverter uses three parallel capacitor banks indicated as "C_{bus}" altogether. The main bank has five high-capacitance electrolytic capacitors to stabilize the DC voltage input to the inverter, with total nominal capacitance $C_c = 390$ μF. The other two banks (one per inverter leg) have 16 ceramic capacitors each, with nominal capacitance $C_{PCB} = 2.2$ μF, to suppress switching over-voltages caused by the PCB trace inductance. The parasitic parameters of the DC bus capacitors were measured experimentally with a vector network analyzer (VNA). The measured values (leakage resistance $R_{bus} = 20$ mΩ, inductance $L_{bus} = 21.2$ nH, and effective capacitance $C^*_{bus} = 375$ μF) were inserted into the circuit simulations to obtain realistic results, focused on measurements around the switching frequency.

The two "LISN" (line impedance stabilization network) blocks in Figures 1 and 2 indicate the points where the feeding impedance network is normalized for the successive measurement of conducted emissions.

To understand the role of the inverter load, it must be considered that the (non-filtered) bridge input current $i_{in}(t)$ corresponds to the rectified waveform of the inverter output current $i_1(t)$ [51–53]. Moreover, due to the presence of a DC bus that fixes the H-bridge input voltage, the inverter can be considered a nearly ideal square-wave voltage source [20]. It is then clear that the inverter load determines $i_1(t)$, which in turn affects $i_{in}(t)$ resulting in the grid current $i_S(t)$ after DC bus filtering.

The input DC link current was used in [54], as well as collecting all the switching phenomena inside the converter, with the possibility of limiting sensing to radiated electromagnetic emissions with an advantage in terms of intrusiveness and practicability, but

limited to open-circuit fault detection. Here, the $i_1(t)$ load current is considered, but many kinds of faults are taken into account.

As a case study, two different situations are considered:

- a resistive load represented by the resistance R; (see Figure 1)
- a resonant WPT network (see Figure 2).

In the former case

$$i_1(t) = \frac{v_1(t)}{R} \tag{1}$$

and the waveform of the output current $i_1(t)$ is the scaled version of the $v_1(t)$ waveform. The spectrum harmonics are thus expected to be the same (with a scaled magnitude). A particular situation arises when the inverter duty cycle is 50%: in this case, the bridge current $i_{in}(t)$ should be a perfect DC waveform. However, the necessary inverter-leg dead times make $i_{in}(t)$ a rectified non-ideal square waveform. When considering the WPT networks, the situation is clearly different. While $v_1(t)$ is still a square voltage waveform, $i_1(t)$ presents a much more smoothed trend depending on the network parameters.

The considered WPT system is composed of two identical magnetically-coupled coils and presents two identical series-connected capacitors tuned as:

$$C = \frac{1}{\omega_0^2 L} \tag{2}$$

where $\omega_0 = 2\pi f_0$ is the resonant angular frequency. The network parameters are summarised in Table 1.

Table 1. WPT system parameters.

Quantity	Symbol	Value
Coil resistance	R	0.1 Ω
Coil self-inductance	L	12.5 µH
Coils mutual inductance	M	5 µH
Compensation capacitance	C	280 nF
Resonance frequency	f_0	85 kHz
Load resistance	R_{load}	2.5 Ω
Source voltage	$\hat{V}_s$	50 V$_{rms}$

In rated operations, the fundamental of $v_1(t)$ oscillates at the WPT network resonant frequency f_0 and $i_1(t)$ is a sinusoidal waveform whose amplitude is determined by the network parameters. The impact of the dead times is thus nullified by the filtering action of the WPT network. For consistent measurement of the input current, the input impedance of the converter is set introducing two LISNs, one for each DC pole of the supply.

The circuits were simulated in LT Spice [55].

3. Fault Diagnosis via Autoregressive Modelling

As mentioned in Section 1, the fundamental target of FD is to detect and identify any type of fault, possibly in the initial phase of occurrence, in order to avoid shutdowns and therefore to be able to plan a system maintenance action in advance.

Two fundamental tasks can be distinguished in an FD strategy: detection and isolation. During the former, the system is monitored for any sign of malfunction, by means of sensors that measure parameters like current, voltage, temperature, pressure, etc. The collected data can indicate the health status of the system: whether it is functioning normally or has developed a fault and an alarm is activated. Nevertheless, the faulty element and the relative fault mode remains unknown. During the latter, the faulty component and corresponding fault mode that has given rise to a fault alarm are identified, and the faulty devices can be segregated, redesigning the converter for continuous and safe operation.

Both real-time sensed capacitor voltage and bus current are commonly used as control variables for the FD. Starting from these quantities, in this Section we describe a simple and effective diagnostic method to cope with the considered open- and short-circuit faults. By taking advantage of the properties of AR modeling, the implementation of the procedures is simple and does not require any prior physical knowledge of the converter parameters, accomplishing both of the tasks described above.

3.1. Autoregressive Modelling

Given N samples $y(1), y(2), \ldots, y(N)$ of the time series $y(t)$, its representation through an AR model is given by

$$y(t) + a_1 y(t-1) + \cdots + a_p y(t-p) = e(t), \tag{3}$$

where $e(t)$ is a zero mean driving white noise process with variance σ_e^2 that can also be seen as a prediction error. In fact, given an estimated model $\hat{a}_1, \hat{a}_2, \ldots, \hat{a}_p$, the optimal one-step ahead prediction $\hat{y}(t)$ of the signal $y(t)$ is computed as follows

$$\hat{y}(t) = -\hat{a}_1 y(t-1) - \hat{a}_2 y(t-2) - \cdots - \hat{a}_p y(t-p). \tag{4}$$

It is worth noting that model (3) can be written in the form

$$y(t) = \frac{e(t)}{A(z^{-1})} \tag{5}$$

where $A(z^{-1}) = 1 + a_1 z^{-1} + \cdots + a_p z^{-p}$ is a polynomial in the unit delay operator z^{-1}, i.e., $z^{-1}y(t) = y(t-1)$. The AR process $y(t)$ can thus be seen as the output of an all-pole filter driven by a white process.

Among the available methods for identifying AR models, the least squares approach is based on the minimization of the sum of the squared prediction errors $J(\theta)$ [35,36]:

$$J(\theta) = \sum_{t=p+1}^{N} (y(t) - \hat{y}(t))^2 = \sum_{t=1}^{N} (y(t) - \varphi^T(t)\theta)^2 \tag{6}$$

where

$$\varphi(t) = \left[-y(t-1) \ -y(t-2) \ \cdots \ -y(t-p) \right]^T \tag{7}$$

$$\theta = \left[a_1 \ a_2 \ \cdots \ a_p \right]^T. \tag{8}$$

The solution is given by:

$$\hat{\theta} = \left(\sum_{t=p+1}^{N} \varphi(t)\varphi^T(t) \right)^{-1} \sum_{t=p+1}^{N} \varphi(t)y(t). \tag{9}$$

An estimate of the additive noise variance σ_e^2 can be computed as follows

$$\hat{\sigma}_e^2 = \frac{1}{N-p} \sum_{t=p+1}^{N} (y(t) - \varphi^T(t)\hat{\theta})^2 = J(\hat{\theta}). \tag{10}$$

Other frequently used approaches are Yule–Walker equations and the Burg algorithm [36,37].

As far as the AR model order p is concerned, the most popular methods for estimating it are the final prediction error criterion (FPE), the Akaike information criterion (AIC), and the Bayesian information criterion (BIC) (also known as MDL, from the minimum description length principle) [36,37]. They are based on the minimization of different cost functions depending on the loss function $J(\hat{\theta})$ and increasing values of the model order p [35–37].

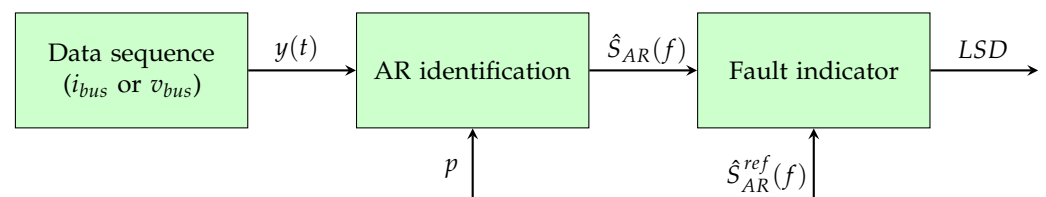### 3.2. Fault Diagnosis Procedure

As mentioned in Section 1, the use of AR models in FD consists of first estimating an AR model of the measured signal $y(t)$ (vibration, current, etc.) and then extracting suitable features from the estimated model to discriminate healthy conditions from faulty ones. An effective way to perform the diagnostics task is to consider the estimated AR power spectral density (PSD) of the signal $y(t)$ [40,44,46], which can be computed from (5):

$$\hat{S}_{AR}(f) = \frac{\hat{\sigma}_e^2}{|\hat{A}(e^{-j2\pi f})|^2} = \frac{\hat{\sigma}_e^2}{|1 + \sum_{k=1}^{p} \hat{a}_k\, e^{-j2k\pi f}|^2}. \tag{11}$$

where $\hat{a}_1, \ldots, \hat{a}_p$ are the estimated model coefficients and $\hat{\sigma}_e^2$ is computed from (10). Essentially, the method consists of estimating an AR PSD during normal operating (healthy conditions) that will be taken as the reference PSD $\hat{S}_{AR}^{ref}(f)$. The reference $\hat{S}_{AR}^{ref}(f)$ is then compared to the PSD $\hat{S}_{AR}(f)$ obtained starting from sequences collected subsequently under healthy or faulty conditions in order to compute an health indicator which is able to solve the FD problem. For instance, the log spectral distance

$$LSD = \frac{1}{N_f} \sum_{k=1}^{N_f} \left(\log \frac{\hat{S}_{AR}(f_k)}{\hat{S}_{AR}^{ref}(f_k)} \right)^2 \tag{12}$$

or other spectral distances can be used to detect signal changes [56], where N_f is the number of frequency bins considered in the evaluation of the power spectral densities. The logarithmic nature of LSD makes it particularly effective when relative differences in PSD amplitude are more important than absolute differences. The proposed fault diagnosis procedure is summarized in Figure 3.

Figure 3. Fault diagnosis procedure. The AR order p and the reference AR PSD $\hat{S}_{AR}^{ref}(f)$ are estimated by using a portion of the healthy signal.

In principle, it would also be possible to evaluate the spectral distance by directly comparing the healthy and defective Fourier spectra. However, theoretical considerations and empirical evidence suggest that the diagnostic process is more difficult w.r.t. AR-based methods, especially for real signals [57–60]. Even when detection is possible, the spectral distances are smaller, complicating their recognition compared to the AR case [59,60]. This is mainly due to the fact that, unlike FFT-based methods, the estimated AR spectra do not involve signal windowing, leading to an improved spectral resolution and preventing the introduction of sidelobes effects [36]. Furthermore, the AR PSD estimation is more robust in the presence of noise, as the effect of noise can be effectively counteracted by increasing the model order or by signal decimation [36,61].

4. Results

The presented technique can identify deviations in the frequency content of the spectra following the occurrence of anomalous situations or in general deviations from nominal or reference conditions. A reference spectrum is thus needed to tune the algorithm and nominal operating conditions are defined.

For a resistive load, the reference is represented by the square waveforms $v_1(t)$ and $i_1(t)$, shown in Figure 4a with the corresponding spectra of $v_{bus}(t)$ and $i_{in}(t)$ shown in

Figure 5a. The voltage $v_1(t)$ presents spikes due to dead times, which are necessary, however, to allow adequate protection against shot-through. The bus voltage and input current have more populated spectra with respect to the ideal one (DC voltage current), which still presents the fundamental component at $2f_0$.

In the case of the WPT system, voltage and current waveforms $v_1(t)$ and $i_1(t)$ are shown in Figure 4b and the spectra of the corresponding $v_{bus}(t)$ and $i_{in}(t)$ are shown in Figure 5b. In this case, the voltage spikes are much more pronounced, due to the resonance they trigger (during the dead time the resonant circuit is left in high terminating impedance conditions).

(**a**) (**b**)
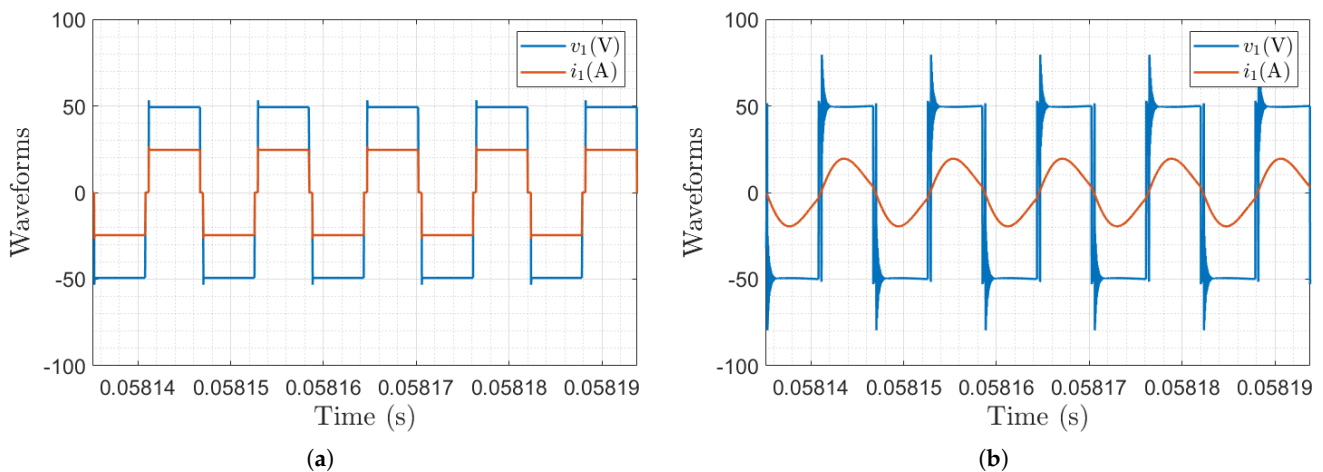
Figure 4. Reference waveforms of the output voltage and current for resistive load: (**a**) common mode, (**b**) differential mode.

(**a**) (**b**)
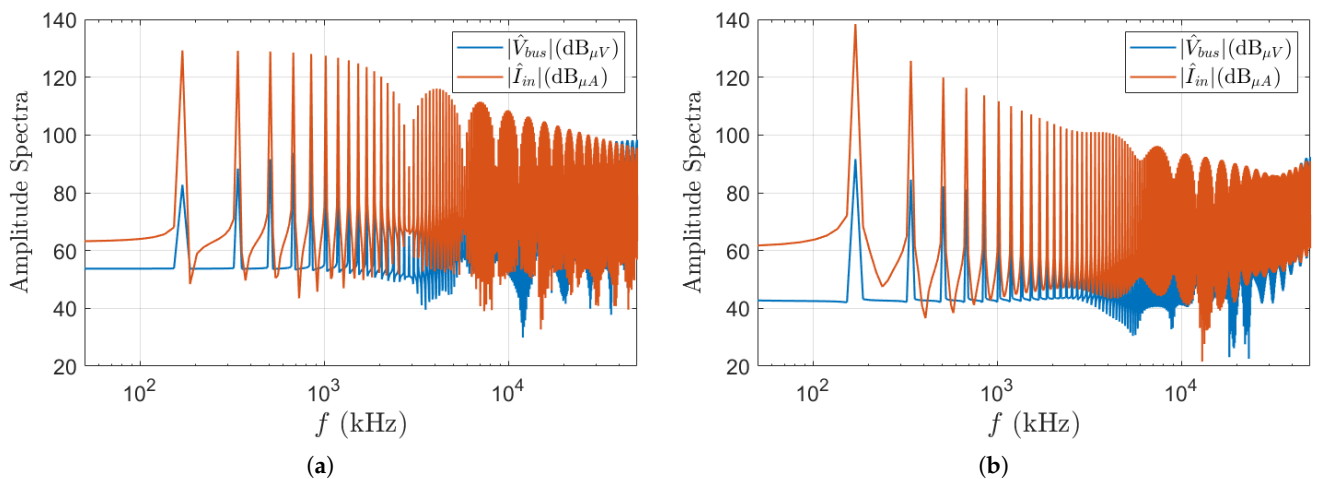
Figure 5. Reference spectra of the output voltage and current for resistive load: (**a**) common mode, (**b**) differential mode.

4.1. Non-Ideal Behavior and Fault Scenarios

As discussed in the introduction, power converters can experience faults during operation and they are mainly related to the switch's electrical conditions and dead times. For both the case studies, namely inverter with resistive load and a WPT system, two main fault scenarios are considered: asymmetric dead time and fault of an inverter semiconductor switch.

4.1.1. Asymmetric Dead Time

At the first degradation, a deviation of the dead time of a leg with respect to the reference value is assumed: the technical justification may be an increased resistance of the

semiconductor driving circuit. Specifically, the dead time of the right leg of the inverter has been increased by 50 %, leading to an asymmetric square input voltage waveform. This type of fault will be denoted as "ASYF".

4.1.2. Switch Fault

As main semiconductor switch faults, open-circuit faults (denoted as "OCFs"), and short-circuit faults (denoted as "SCFs") of the S_4 switch have been considered for both the case studies (resistive load and a WPT system). Moreover, to test the sensitivity of the proposed fault-diagnosis methodology, increased values of the S_4 switch resistance R_{sw4} by 10 and 100 times have also been introduced.

In the following subsections, we describe the results obtained by using the FD technique introduced in Section 3.2 applied to both power converters (so feeding both the resistive load and a WPT system).

4.2. AR-based FD: H-Bridge Inverter with Resistive Load

The H-bridge inverter with resistive load has been considered first (see Figure 1). The signal that was used to extract the AR models is the bus current $i_{bus}(t)$. Figure 6 shows the time domain waveform of $i_{bus}(t)$ in the nominal and the faulty conditions.

According to the procedure described in Section 3.2, a suitable AR model order has been estimated by using sequences of $i_{bus}(t)$ collected under normal operating conditions.

Both the FPE and MDL criteria lead to the selection of the order $p = 300$. Then, AR models of order p have been identified through the least squares method and the associated power spectral densities have been computed from (11).

Figure 7a–c compare the PSDs related to the reference condition (red line) with those obtained in the three fault scenarios (blue line). These figures show that the three faulty conditions can be clearly distinguished from the nominal condition.

To test the effectiveness and robustness of the proposed approach under non-ideal conditions, the FD procedure has been applied to noisy bus current signals obtained by adding white noise to the original signals in all conditions. The variance in the noise has been chosen to set a signal-to-noise ratio $SNR = 50$ dB in the healthy condition. White noise sequences with the same variance have been added to the signals related to the faulty conditions. The diagnostic procedure has been implemented as follows:

1. First, a reference AR model is estimated by using a portion of the healthy signal and the corresponding PSD $\hat{S}_{AR}^{ref}(f)$ is computed from (11).
2. Then, the remaining part of the healthy data and the faulty data are segmented into overlapping frames of length $N = 10{,}000$ samples. For each sequence, an AR model of order $p = 300$ is estimated and the associated PSD $\hat{S}_{AR}(f)$ is computed.
3. Finally, each current PSD is compared with the reference one through the health indicator (12).

Figure 8 shows the evolution of the LSD health indicator for the H-bridge converter with resistive load for the different considered fault conditions (from left to right: healthy, OCF, ASYF, and SCF).

Within each interval, different signal segments (frames) of N samples are considered and the value of the spectral distance (12) is calculated by comparing the PSDs obtained from each (healthy or faulty) frame with the reference one. This procedure follows the same philosophy as the short-time Fourier transform. In fact, AR identification (and the associated AR spectral estimation) is performed on short segments of measured data and the signal is assumed to be weakly stationary only within each frame. This allows taking into account phenomena such as wear and fatigue.
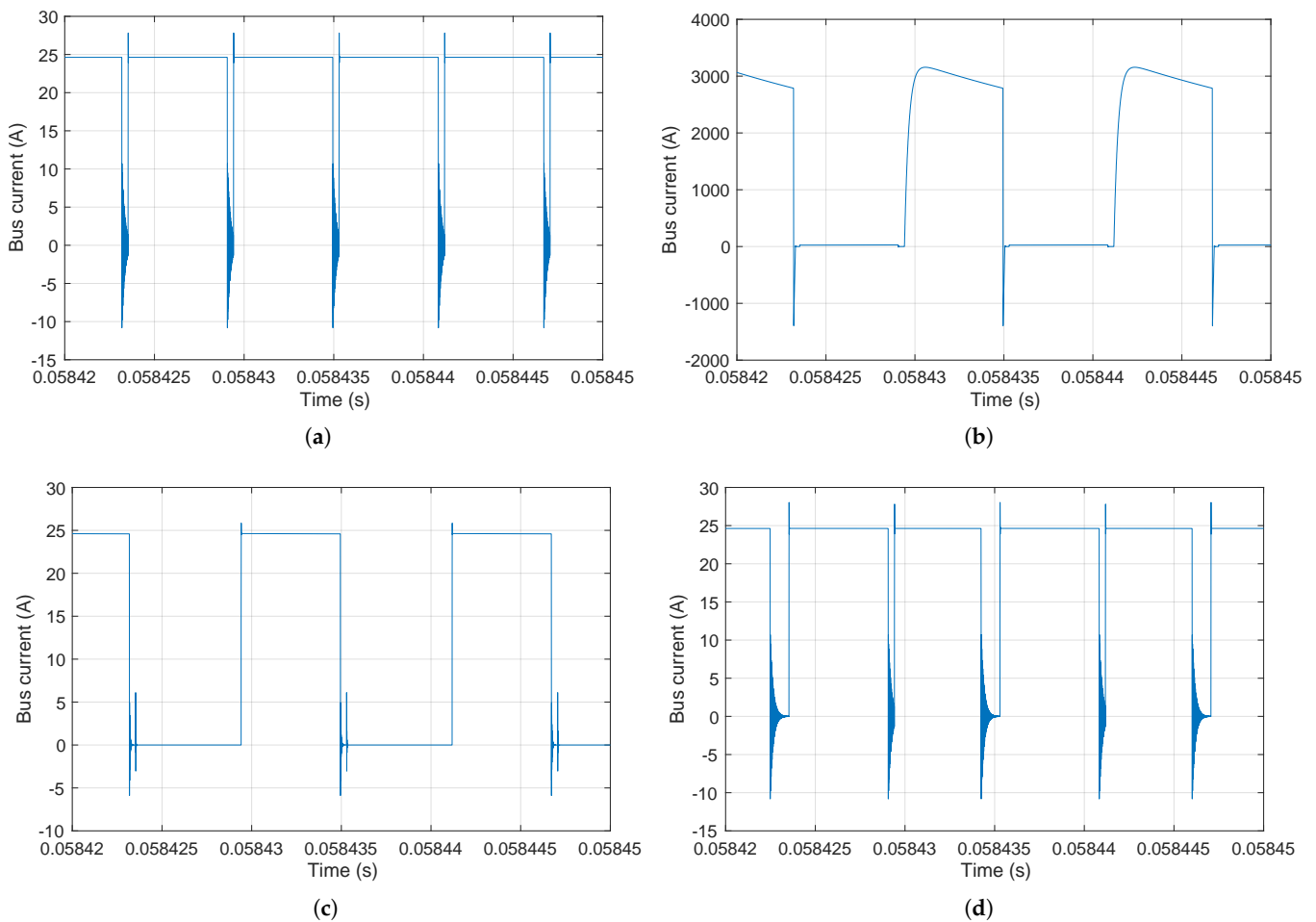
Figure 6. The time domain waveform of $i_{bus}(t)$ in four different conditions for the H-bridge inverter with resistive load: (**a**) healthy; (**b**) short circuit; (**c**) open circuit; (**d**) asymmetric input voltage.

Two observations should be made at this point.

- The values corresponding to the four situations are different and, within each interval, the value of the indicator exhibits very small variations; this is consistent with the fact that the processed signal is due to the same fault type.
- Furthermore, the value of the spectral distance in the healthy case also remains almost constant and lower than in the other cases (by at least an order of magnitude), making the detection clear.

The health indicator based on the AR PSD shows a high sensitivity to different conditions, which allows robust detection thresholds to be defined. In other words, even much smaller deviations of parameters can be detected, such as in the case of incipient faults. This feature makes the proposed indicator particularly suitable for online condition monitoring of power converters.

The aforementioned procedure has been then further tested by considering a more severe SNR condition. More precisely, the bus current signals of the four conditions have been corrupted by additive white noise with increased variance leading to $SNR = 20\,\text{dB}$ in the healthy status. In this case, the evolution of the healthy indicator LSD is shown in Figure 9. It can be seen that the proposed approach is robust with respect to the presence of noise even though the relative distance (LSD values) between faulty and healthy conditions decreases as expected, in particular for the ASYC fault. Although the obtained results are satisfactory, detection capabilities in the presence of noise can be further improved in a simple way by increasing the order of the AR model [36]. Nevertheless, if a signal

is acquired with a sufficiently high sampling rate, a more effective solution consists of decimating the signal before the identification step [61]. This approach also allows for better resolution with a lower-order model, approximately equal to $p' \cong p/D$ if D is the decimation factor. Figure 10 shows the results obtained by decimating all considered signals by a factor $D = 5$ and considering AR models of order $p' = 50$ instead of $p = 300$. By comparing Figures 9 and 10, it is easy to see how the decimation decreased the LSD value in the absence of faults, suggesting an even greater similarity between the PSDs of the frames considered, and significantly increasing the relative distance with the ASYF case (frames 1 and 3), thus ensuring a more robust detection.

(a)

(b)

(c)
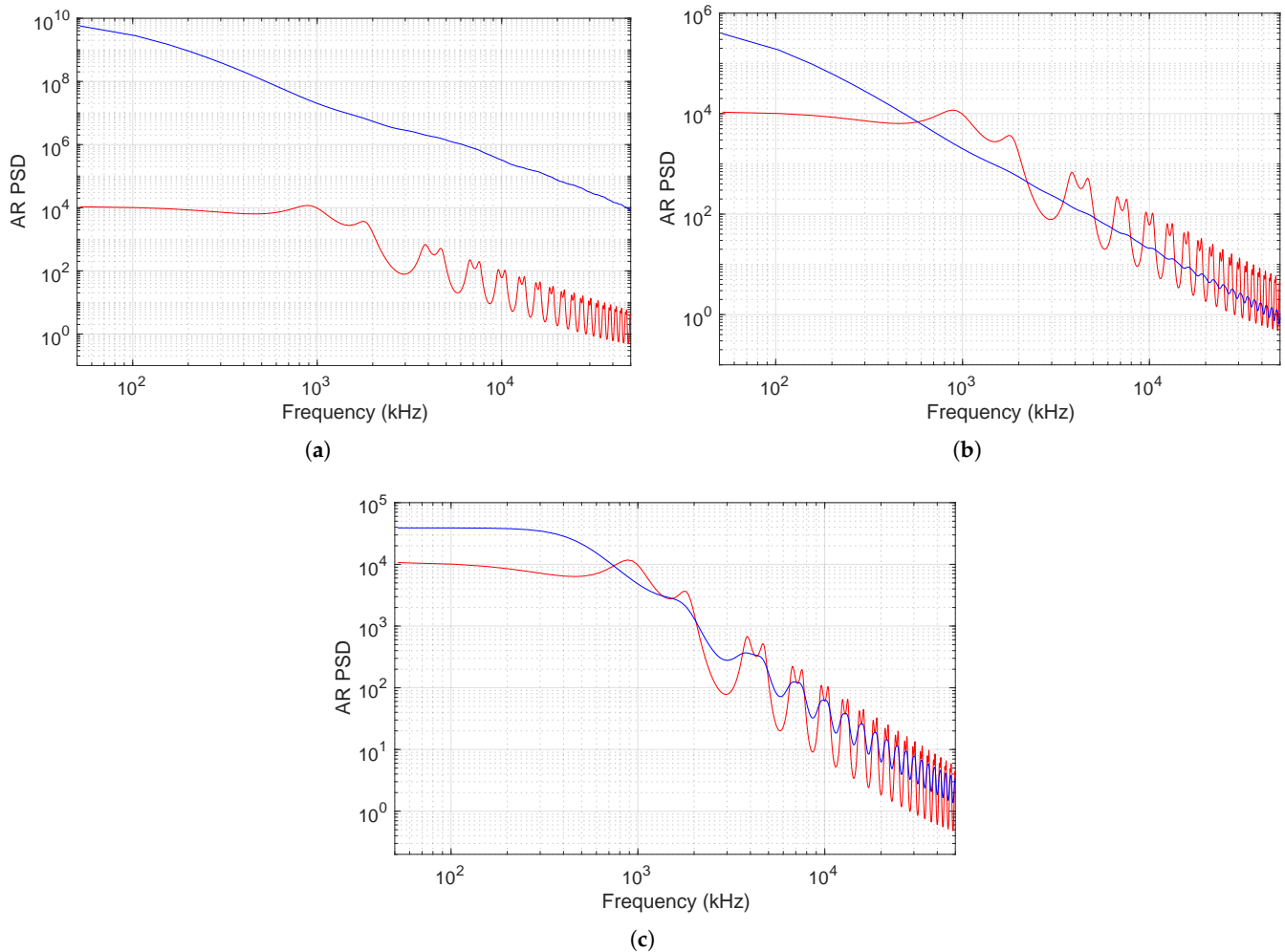
Figure 7. Comparison among the estimated AR power spectral densities in the different conditions for the H-bridge inverter with resistive load. The reference (healthy) AR PSD $\hat{S}_{AR}^{ref}(f)$ (red) is compared with the AR PSDs estimated in faulty conditions (blue): (**a**) healthy vs. short circuit; (**b**) healthy vs. open circuit; (**c**) healthy vs. asymmetric input voltage.

To show the ability of the method to "capture" more subtle faults, increased values of the S4 switch resistance R_{sw4} by factors of 10 and 100 have been considered. This allows one to simulate the degradation of the converter status from healthy to an open-circuit fault ($R_{sw4} \to \infty$). The proposed diagnostic procedure has been applied to sequences corrupted by additive white noise with $SNR = 50\,\text{dB}$ and the AR model order is set to $p = 300$.

The obtained results are summarized in Figure 11, which shows clearly different *LSD* levels in the following four conditions: healthy, $10R_{sw4}$, $100R_{sw4}$, and open circuit. Even in this case, the difference between the R_{sw4} healthy and $10R_{sw4}$ levels is acceptable for detection but smaller than in previous cases. It is worth noting that the sensitivity of

the health indicator can also be significantly improved in this case by signal decimation. Figure 12 reports the LSD computed from AR models of order $p' = 50$, starting from signals decimated by $D = 5$. It can be easily noted the large increase in the relative distance between the healthy and the first fault condition (resistance value increased by 10).

This example confirms that the proposed approach can be adopted for the condition monitoring of the converter because of its good detection ability.
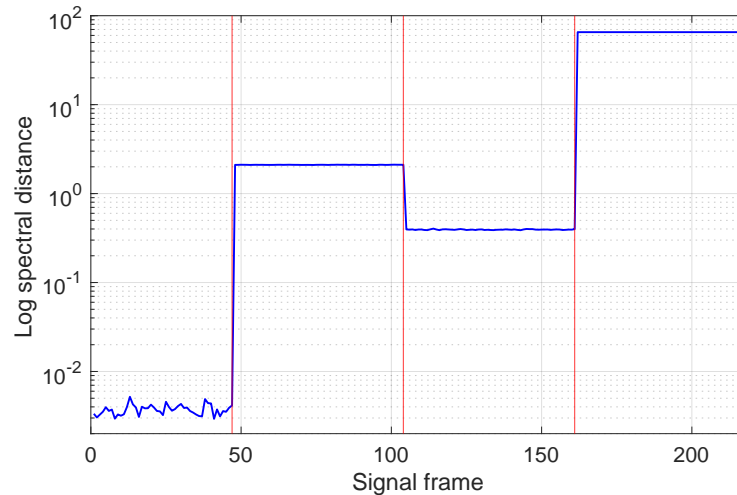
Figure 8. Evolution of the log spectral distance (LSD indicator) computed from AR PSD in the presence of additive noise with $SNR = 50\,\text{dB}$ in four different conditions (resistive load). From left to right: healthy, OCF, ASYF, and SCF. The red lines indicate the different signal segments (frames) of N samples corresponding to the four different conditions.
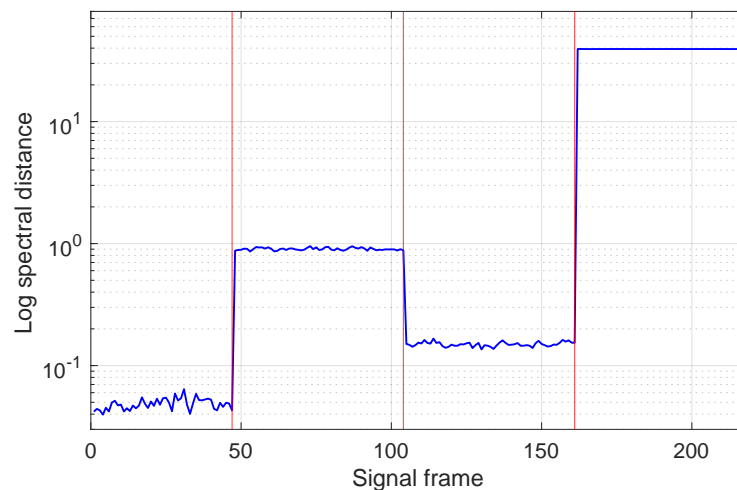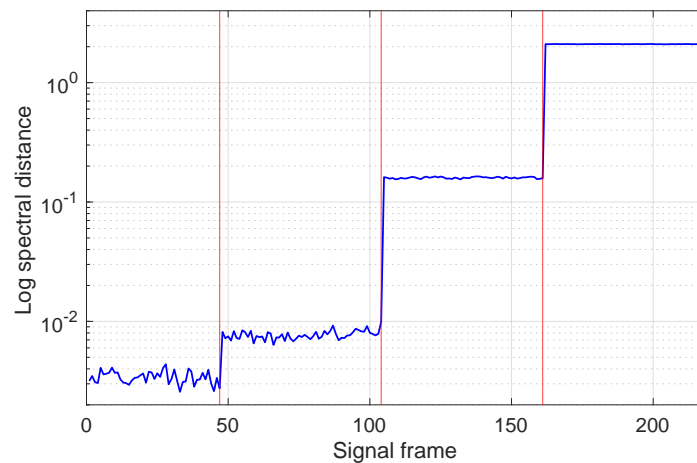

Figure 9. Evolution of the log spectral distance (LSD indicator) computed from the AR PSD in the presence of additive noise with $SNR = 20\,\text{dB}$ in four different conditions (in the case of resistive load). From left to right: healthy, OCF, ASYF, and SCF. The red lines indicate the different signal segments (frames) of N samples corresponding to the four different conditions.

It is worthwhile to highlight that the method also shows very good performance when the AR models are extracted from the bus voltage. As examples, Figures 13 and 14 show the evolution of the health indicator obtained from identified AR models of order $p = 300$. Both the cases of OCF, ASYF, SCF, and increased SW4 switch resistance are shown. It seems that $v_{bus}(t)$ leads to an health LSD indicator even more sensitive to the different conditions w.r.t. that computed starting from $i_{bus}(t)$.
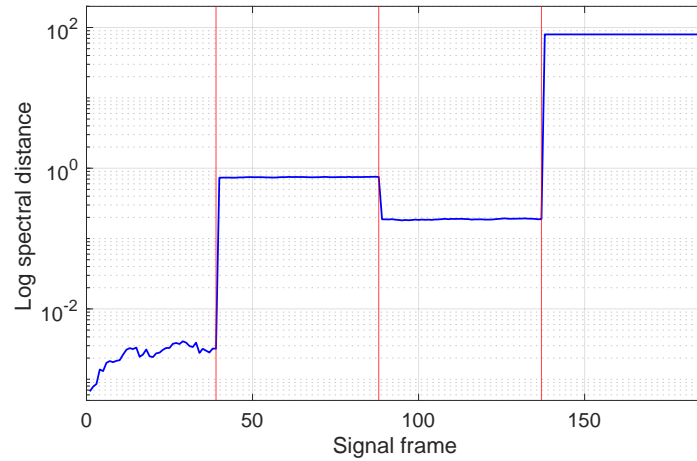
Figure 10. Evolution of the log spectral distance (LSD indicator) computed for the AR PSD in the presence of additive noise with $SNR = 20\,\text{dB}$ in four different conditions (in the case of resistive load). From left to right: healthy, OCF, ASYF, and SCF. All signals were decimated by a factor of $D = 5$ and AR models of order $p' = 50$ have been estimated. The red lines indicate the different signal segments (frames) of N samples corresponding to the four different conditions.

Figure 11. Evolution of the log spectral distance (LSD indicator) computed from the AR PSD in the presence of additive noise with $SNR = 50\,\text{dB}$ in four different conditions (in the case of resistive load). From left to right: healthy, $10R_{sw4}$, $100R_{sw4}$, and open circuit. The red lines indicate the different signal segments (frames) of N samples corresponding to the four different conditions.

### 4.3. AR-Based FD: H-Bridge Inverter Supplying a WPT System

This subsection describes the results obtained by applying the proposed diagnosis procedure in Section 3.2 to the H-bridge inverter supplying the WPT system (see Figure 2). The bus current $i_{bus}(t)$ is the signal that was used to extract the AR models. Figure 15 shows the time domain waveform of $i_{bus}(t)$ in the nominal and faulty conditions.

Firstly, a suitable AR model order has been estimated by using sequences related to healthy conditions. Both the FPE and MDL criteria lead to the selection of the order $p = 160$. Then, AR model models of order $p = 160$ have been identified through the least squares method and the associated power spectral densities have been computed from (11).

Figure 16a–c compares the PSDs related to the reference condition (red line) with those obtained in the three fault scenarios (blue line). These figures show that the three faulty conditions can be clearly distinguished form the healthy status.

Following the same lines described in Section 4.2, the procedure has been applied to noisy signals obtained by adding white noise to the original signals in all conditions. Again, a reference AR power spectral density $\hat{S}_{AR}^{ref}(f)$ is first determined from a portion of the healthy data. Then, the remaining healthy data and the faulty data are divided

into overlapping frames of length $N = 10{,}000$ samples, each of which leads to an AR PSD estimate $\hat{S}_{AR}(f)$. For each frame, the PSD $\hat{S}_{AR}(f)$ is compared with the reference one through the health indicator (12). Figure 17 shows the evolution of the LSD health indicator in the different conditions (healthy, OCF, ASYF, SCF) for $SNR = 50\,\text{dB}$ whereas Figure 18 refers to $SNR = 20\,\text{dB}$. Figure 19 reports the evolution of LSD for different values of the SW4 switch resistance: R_{sw4} healthy, $10R_{sw4}$, $100R_{sw4}$, and $R_{sw4} \to \infty$ (open circuit). The ability of the method to distinguish the different status of the converter is also clearly confirmed for the case of the H-bridge inverter supplying a WPT system.
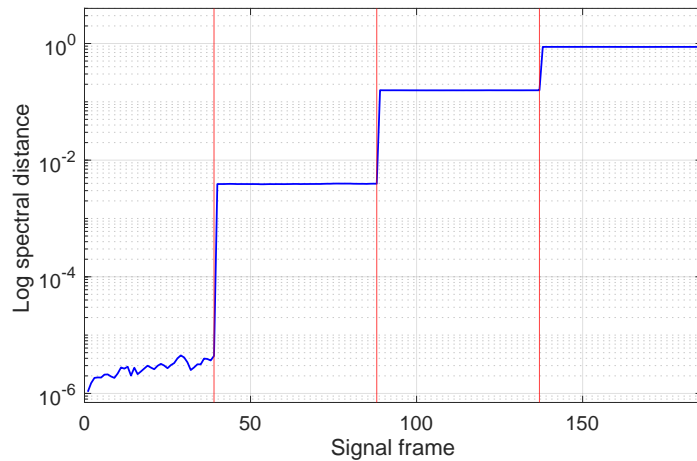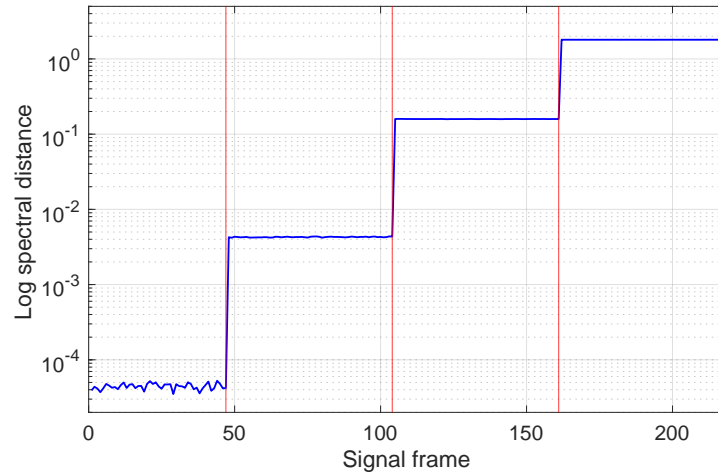

Figure 12. Evolution of the log spectral distance (LSD indicator) computed from the AR PSD in the presence of additive noise with $SNR = 50\,\text{dB}$ in four different conditions (in the case of resistive load). From left to right: healthy, $10R_{sw4}$, $100R_{sw4}$, and open circuit. All signals have been decimated by $D = 5$ and AR models of order $p' = 50$ have been estimated. The red lines indicate the different signal segments (frames) of N samples corresponding to the four different conditions.
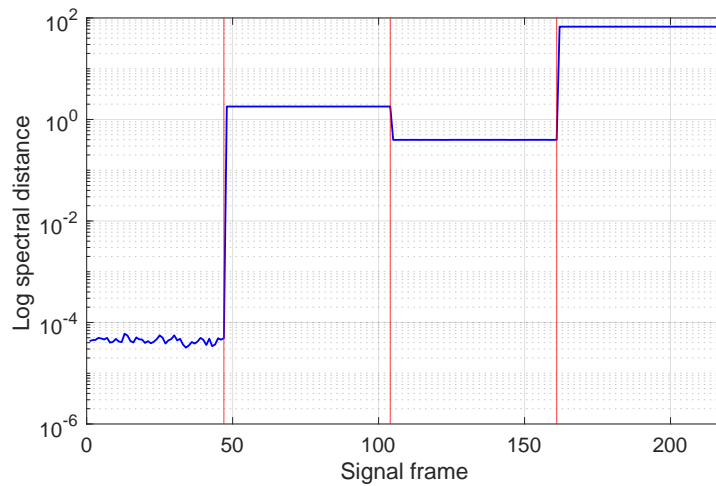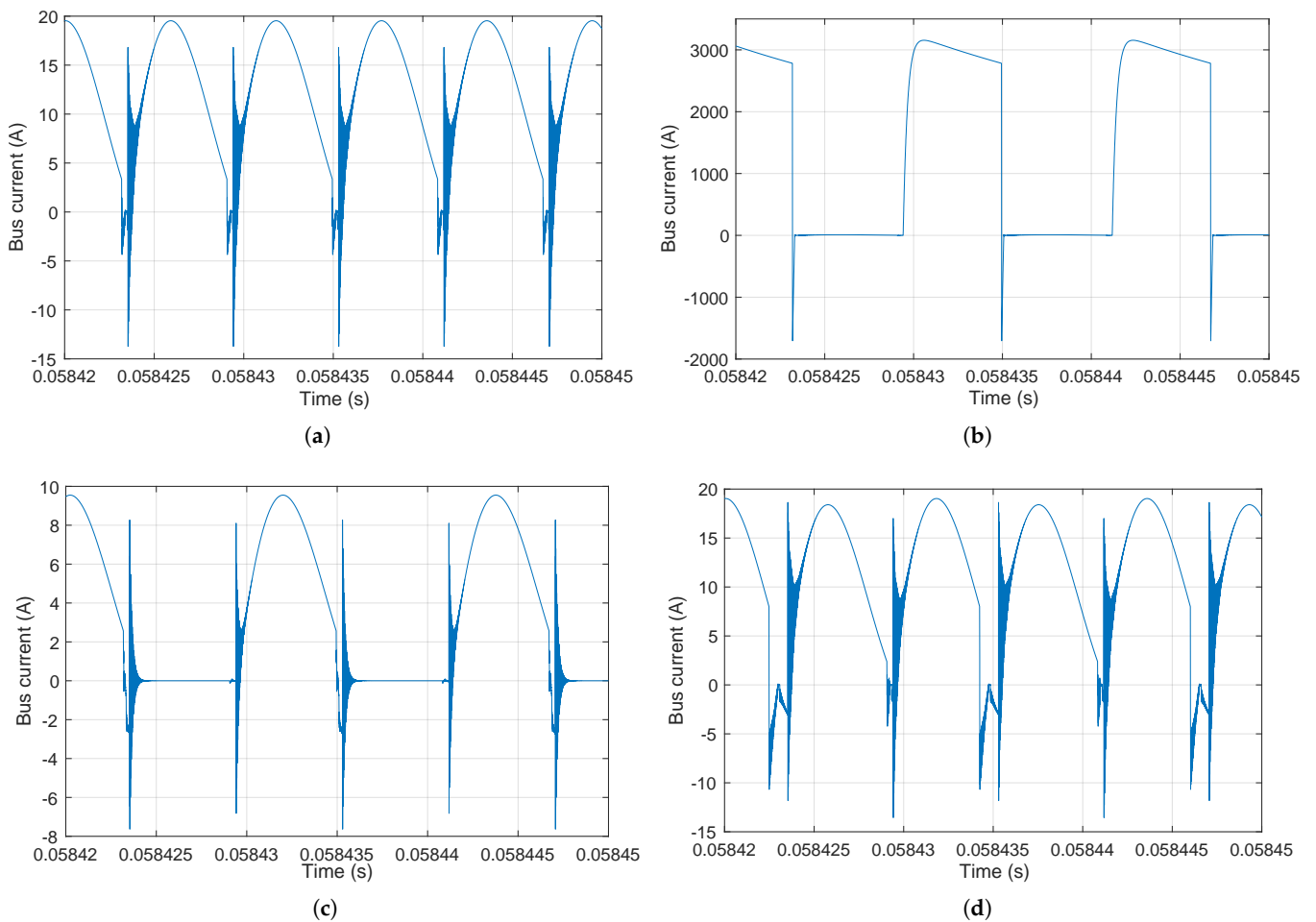

Figure 13. Evolution of the log spectral distance (LSD indicator) computed from the AR PSD in the presence of additive noise with $SNR = 50\,\text{dB}$ in four different conditions (resistive load). From left to right: healthy, OCF, ASYF, and SCF. AR models estimated from the bus voltage $v_{bus}(t)$. The red lines indicate the different signal segments (frames) of N samples corresponding to the four different conditions.

The same conclusion can be stated by observing Figures 20 and 21, which show the evolution of the LSD indicator computed from AR models estimated from the bus voltage signal $v_{bus}(t)$.
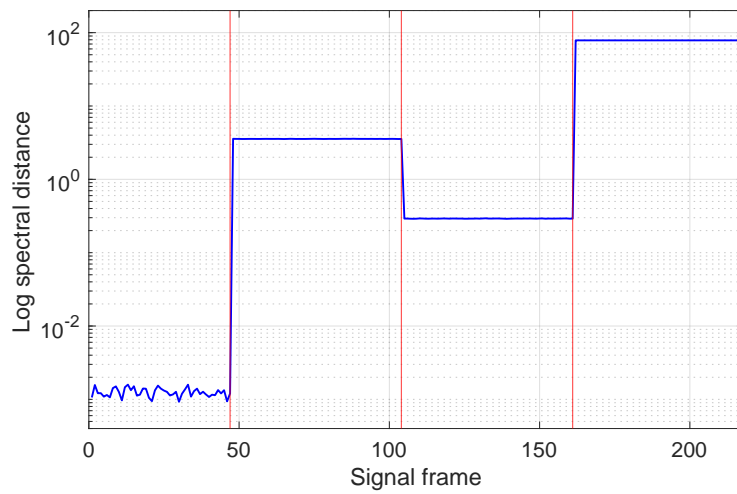
Figure 14. Evolution of the log spectral distance (LSD indicator) computed from the AR PSD in the presence of additive noise with $SNR = 50\,\text{dB}$ in four different conditions (in the case of resistive load). From left to right: healthy, $10R_{sw4}$, $100R_{sw4}$, and open circuit. AR models estimated from the bus voltage $v_{bus}(t)$. The red lines indicate the different signal segments (frames) of N samples corresponding to the four different conditions.

(**a**)

(**b**)

(**c**)

(**d**)

Figure 15. Time domain waveform of $i_{bus}(t)$ in four different conditions for the H-bridge inverter with the WPT system: (**a**) healthy; (**b**) short circuit; (**c**) open circuit; (**d**) asymmetric input voltage.
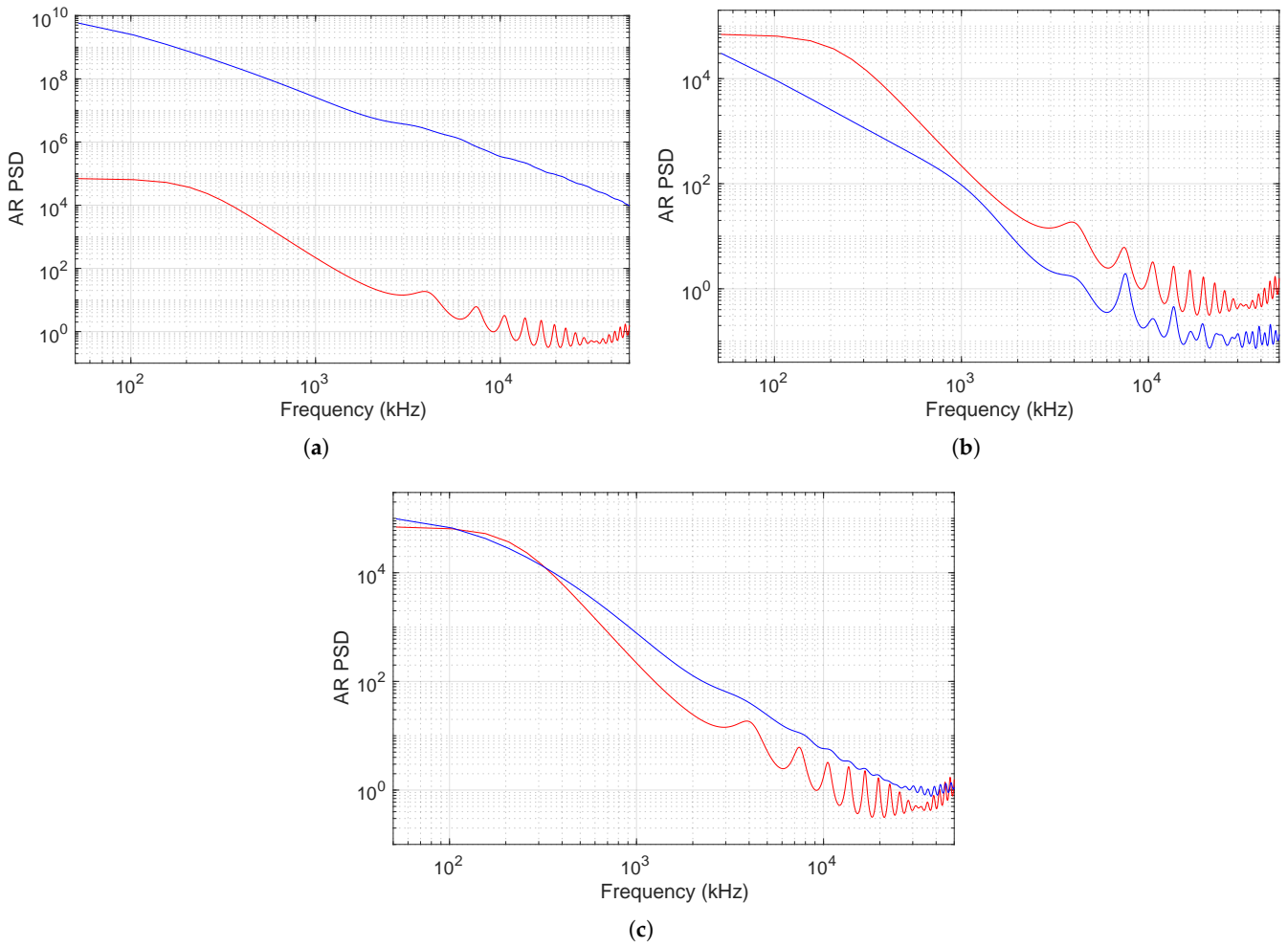
Figure 16. Comparison of the estimated AR power spectral densities in the different conditions for the the H-bridge inverter with the WPT system. The reference (healthy) AR PSD $\hat{S}_{AR}^{ref}(f)$ (red) is compared with the AR PSD estimated in faulty conditions (blue): (**a**) healthy vs. short circuit; (**b**) healthy vs. open circuit; (**c**) healthy vs. asymmetric input voltage.

Figure 17. Evolution of the log spectral distance (LSD indicator) computed from AR PSD in the presence of additive noise with $SNR = 50\,\text{dB}$ in four different conditions (inverter with a WPT system). From left to right: healthy, OCF, ASYF, and SCF. The red lines indicate the different signal segments (frames) of N samples corresponding to the four different conditions.
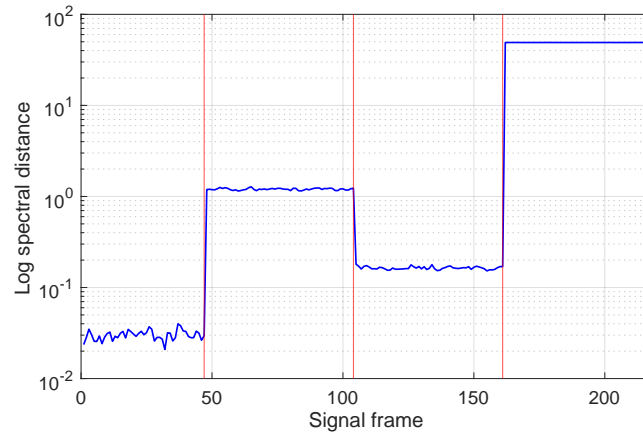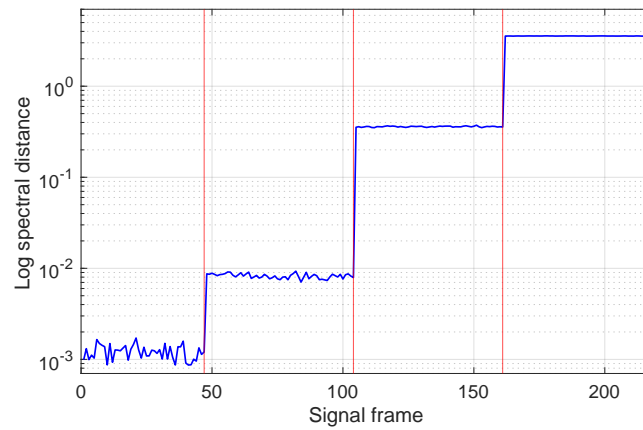
Figure 18. Evolution of the log spectral distance (LSD indicator) computed from AR PSDs in the presence of additive noise with $SNR = 20\,\text{dB}$ in four different conditions (inverter with the WPT system). From left to right: healthy, OCF, ASYF, and SCF. The red lines indicate the different signal segments (frames) of N samples corresponding to the four different conditions.
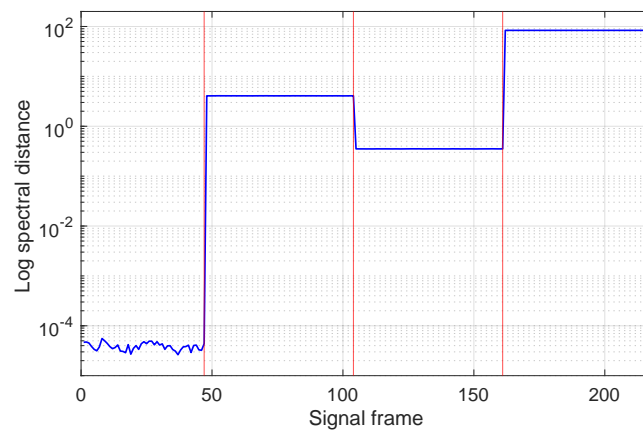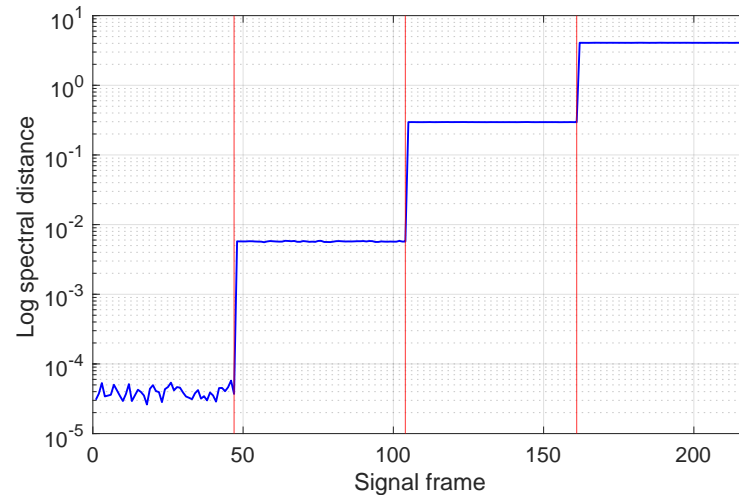

Figure 19. Evolution of the log spectral distance (LSD indicator) computed from the AR PSDs in the presence of additive noise with $SNR = 50\,\text{dB}$ in four different conditions (inverter with the WPT system). From left to right: R_{sw4} healthy, $10R_{sw4}$, $100R_{sw4}$, SW4 switch open circuit. The red lines indicate the different signal segments (frames) of N samples corresponding to the four different conditions.

Figure 20. Evolution of the log spectral distance (LSD indicator) computed from the AR PSD in the presence of additive noise with $SNR = 50\,\text{dB}$ in four different conditions (inverter with the WPT system). From left to right: healthy, OCF, ASYF, and SCF. AR models estimated from the bus voltage $v_{bus}(t)$. The red lines indicate the different signal segments (frames) of N samples corresponding to the four different conditions.

Figure 21. Evolution of the log spectral distance (LSD indicator) computed from the AR PSD in the presence of additive noise with $SNR = 50\,\text{dB}$ in four different conditions (inverter with the WPT system): R_{sw4} healthy, $10R_{sw4}$, $100R_{sw4}$, and open circuit. AR models estimated from the bus voltage $v_{bus}(t)$. The red lines indicate the different signal segments (frames) of N samples corresponding to the four different conditions.

5. Conclusions

In this work, a diagnostic technique for power converters that exploits auto-regressive modelling was proposed and analyzed. Its effectiveness was demonstrated by considering a converter with H-bridge topology feeding a resistive load as the first case, and a resonant WPT system as the second case. For both cases, fault situations with asymmetric dead time and failure on one of the switches were emulated.

For both failure cases and for both systems considered, the technique proved capable of detecting the failure. To evaluate its robustness, noise was also introduced. With low-order AR models (i.e., $p = 50$) and signals with low sampling frequency (typical of a low-cost implementation), the technique proved to be robust. Its accuracy was also tested by hypothesizing failure cases in which the resistance of a switch was increased by 10 and 100 times, always in the presence of noise. Again, the algorithm was able to determine the failure conditions robustly. This confirms that the proposed approach can be adopted for monitoring the health conditions of converters and the degradation state of the components, even during real-time operation, to warn of possible faults at an early stage.

An additional method to further validate the proposed procedure is the execution of tests on real electronic circuits under different environmental and operating conditions, including various amounts of noise, both colored and white. The use of input–output models, such as ARX models, is also certainly of interest and could be another thread to investigate.

Author Contributions: Conceptualization, R.D., L.S., M.S., N.S. and A.M.; Methodology, R.D., L.S., M.S., N.S. and A.M.; Software, R.D., L.S., M.S., N.S. and A.M.; Validation, R.D., L.S., M.S., N.S. and A.M.; Formal analysis, R.D., L.S., M.S., N.S. and A.M.; Investigation, R.D., L.S., M.S., N.S. and A.M.; Resources, R.D., L.S., M.S., N.S. and A.M.; Data curation, R.D., L.S., M.S., N.S. and A.M.; Writing—original draft, R.D., L.S., M.S., N.S. and A.M.; Writing—review & editing, R.D., L.S., M.S., N.S. and A.M.; Visualization, R.D., L.S., M.S., N.S. and A.M.; Supervision, R.D., L.S., M.S., N.S. and A.M.; Project administration, R.D., L.S., M.S., N.S. and A.M.; Funding acquisition, R.D., L.S., M.S., N.S. and A.M. All authors have read and agreed to the published version of the manuscript.

Data Availability Statement: The original contributions presented in the study are included in the article; further inquiries can be directed to the corresponding author.

Conflicts of Interest: The authors declare no conflicts of interest. The funders had no role in the design of the study; in the collection, analyses, or interpretation of data; in the writing of the manuscript; or in the decision to publish the results.

References

1. Kumar, D.; Zare, F.; Ghosh, A. DC Microgrid Technology: System Architectures, AC Grid Interfaces, Grounding Schemes, Power Quality, Communication Networks, Applications, and Standardizations Aspects. *IEEE Access* **2017**, *5*, 12230–12256. [CrossRef]
2. Bleilevens, R.; Priebe, J.; Wehbring, N.; Moser, A. Reliability Analysis of DC Distribution Grids. In Proceedings of the 2019 54th International Universities Power Engineering Conference (UPEC), Bucharest, Romania, 3–6 September 2019. [CrossRef]
3. Zheng, K.; Yao, X.; Wang, W. Reliability Evaluation of Smart DC Microgrid. In *Communications in Computer and Information Science*; Springer International Publishing: Cham, Switzerland, 2022; pp. 595–605. [CrossRef]
4. Weiss, R.; Ott, L.; Boeke, U. Energy efficient low-voltage DC-grids for commercial buildings. In Proceedings of the 2015 IEEE First International Conference on DC Microgrids (ICDCM), Atlanta, GA, USA, 7–10 June 2015. [CrossRef]
5. Weckmann, S.; Sauer, A. DC Micro Grid for Energy Efficient and Flexible Production. *Procedia Manuf.* **2019**, *39*, 655–664. [CrossRef]
6. Wang, H.; Pei, X.; Wu, Y.; Xiang, Y.; Kang, Y. Switch Fault Diagnosis Method for Series-Parallel Forward DC-DC Converter System. *IEEE Trans. Ind. Electron.* **2019**, *66*, 4684–4695. [CrossRef]
7. Chen, F.; Zhong, Q.; Zhang, H.; Zhu, M.; Müller, S.; Meyer, J.; Huang, W. Survey of harmonic and supraharmonic emission of fast charging stations for electric vehicles in China and Germany. In Proceedings of the 26th International Conference and Exhibition on Electricity Distribution (CIRED), Online Conference, Nanjing, China, 24–27 August 2022; Institution of Engineering and Technology: Stevenage, UK, 2021. [CrossRef]
8. Mariscotti, A. Harmonic and Supraharmonic Emissions of Plug-In Electric Vehicle Chargers. *Smart Cities* **2022**, *5*, 496–521. [CrossRef]
9. Elsayed, A.T.; Mohamed, A.A.; Mohammed, O.A. DC microgrids and distribution systems: An overview. *Electr. Power Syst. Res.* **2015**, *119*, 407–417. [CrossRef]
10. Hu, K.W.; Liaw, C.M. Incorporated operation control of DC microgrid and electric vehicle. *IEEE Trans. Ind. Electron.* **2016**, *63*, 202–215. [CrossRef]
11. Baros, D.; Voglitsis, D.; Papanikolaou, N.P.; Kyritsis, A.; Rigogiannis, N. Wireless Power Transfer for Distributed Energy Sources Exploitation in DC Microgrids. *IEEE Trans. Sustain. Energy* **2019**, *10*, 2039–2049. [CrossRef]
12. Simonazzi, M.; Sandrolini, L.; Mariscotti, A. Receiver–Coil Location Detection in a Dynamic Wireless Power Transfer System for Electric Vehicle Charging. *Sensors* **2022**, *22*, 2317. [CrossRef]
13. Aviña-Corral, V.; Rangel-Magdaleno, J.d.J.; Barron-Zambrano, J.H.; Rosales-Nuñez, S. Review of fault detection techniques in power converters: Fault analysis and diagnostic methodologies. *Measurement* **2024**, *234*, 114864. [CrossRef]
14. Collin, A.J.; Femine, A.D.; Landi, C.; Langella, R.; Luiso, M.; Testa, A. The Role of Supply Conditions on the Measurement of High-Frequency Emissions. *IEEE Trans. Instrum. Meas.* **2020**, *69*, 6667–6676. [CrossRef]
15. Mariscotti, A.; Sandrolini, L.; Pasini, G. Variability Caused by Setup and Operating Conditions for Conducted EMI of Switched Mode Power Supplies Over the 2–1000 kHz Interval. *IEEE Trans. Instrum. Meas.* **2022**, *71*, 1501009. [CrossRef]
16. Iqbal, M.N.; Kutt, L.; Asad, B.; Shabbir, N. Impact of Cable Impedance on the Harmonic Emission of LED Lamps. In Proceedings of the 2020 21st International Scientific Conference on Electric Power Engineering (EPE), Prague, Czech Republic, 19–21 October 2020. [CrossRef]
17. Bollen, M.; Ronnberg, S.; Hooshyar, H. Spread of high frequency current emission. In Proceedings of the 22nd International Conference and Exhibition on Electricity Distribution (CIRED 2013), Stockholm, Sweden, 10–13 June 2013; Institution of Engineering and Technology: Stevenage, UK, 2013. [CrossRef]
18. Suzuki, M.; Ogawa, K.; Shijo, T.; Kanekivo, Y.; Inoue, K.; Ogura, K.; Obayashi, S.; Ishida, M. Conducted Emission in an 85 kHz, 50 kW WPT System with Opposite-Phase Transfer and Spread Spectrum. In Proceedings of the 2019 IEEE PELS Workshop on Emerging Technologies: Wireless Power Transfer (WoW), London, UK, 18–21 June 2019; pp. 1–4. [CrossRef]
19. Stepins, D.; Zakis, J.; Audze, J.; Husev, O.; Pakhaliuk, B.; Shevchenko, V. Reduction of Conducted Emissions Generated by WPT Systems with Multilevel Inverters using Spread Spectrum Approach. In Proceedings of the IECON 2020 the 46th Annual Conference of the IEEE Industrial Electronics Society, Singapore, 18–21 October 2020; pp. 3924–3929. [CrossRef]
20. Simonazzi, M.; Campanini, A.; Sandrolini, L.; Rossi, C. Design Procedure Based on Maximum Efficiency for Wireless Power Transfer Battery Chargers with Lightweight Vehicle Assembly. *Energies* **2021**, *15*, 70. [CrossRef]
21. Simonazzi, M.; Sandrolini, L.; Campanini, A. Input Current of H-bridge Inverters with Asymmetric Switch Parameters for Wireless Power Transfer Applications. In Proceedings of the 2023 IEEE 17th International Conference on Compatibility, Power Electronics and Power Engineering (CPE-POWERENG), Tallinn, Estonia, 14–16 June 2023; pp. 1–5. [CrossRef]
22. Han, R.; Wang, R.; Zeng, G. Fault Diagnosis Method of Power Electronic Converter Based on Broad Learning. *Complexity* **2020**, *2020*, 7463291. [CrossRef]
23. Januszewski, S.; Kociszewska-Szczerbik, M.; Swiaiek, H.; Swiatek, G. Semiconductor Device Failures in Power Converter Service Conditions. *EPE J.* **1998**, *7*, 12–17. [CrossRef]

24. Valentine, N.; Das, D.; Sood, B.; Pecht, M. Failure Analyses of Modern Power Semiconductor Switching Devices. *IMAPSource Proc.* **2015**, *2015*, 690–695. [CrossRef]
25. Hanif, A.; Yu, Y.; DeVoto, D.; Khan, F. A Comprehensive Review Toward the State-of-the-Art in Failure and Lifetime Predictions of Power Electronic Devices. *IEEE Trans. Power Electron.* **2019**, *34*, 4729–4746. [CrossRef]
26. Fuchs, F. Some diagnosis methods for voltage source inverters in variable speed drives with induction machines—A survey. In Proceedings of the IECON'03. 29th Annual Conference of the IEEE Industrial Electronics Society (IEEE Cat. No.03CH37468), Roanoke, VA, USA, 2–6 November 2003; Volume 2, pp. 1378–1385. [CrossRef]
27. Dhumale, R.; Lokhande, S. Neural Network Fault Diagnosis of Voltage Source Inverter under variable load conditions at different frequencies. *Measurement* **2016**, *91*, 565–575. [CrossRef]
28. Zhao, H.; Cheng, L. Open-Switch Fault-Diagnostic Method for Back-to-Back Converters of a Doubly Fed Wind Power Generation System. *IEEE Trans. Power Electron.* **2018**, *33*, 3452–3461. [CrossRef]
29. Mullali Kunnontakath Puthiyapurayil, M.R.; Nadir Nasirudeen, M.; Saywan, Y.A.; Ahmad, M.W.; Malik, H. A Review of Open-Circuit Switch Fault Diagnostic Methods for Neutral Point Clamped Inverter. *Electronics* **2022**, *11*, 3169. [CrossRef]
30. Lee, J.; Choi, H.G.; Lee, K. Advanced Fault Diagnosis in Power Electronics: Switch Open Faults in DC-Link Shunt Sensor-Less Drives. *J. Electr. Eng. Technol.* **2024**. [CrossRef]
31. Isermann, R. Model-based fault-detection and diagnosis – status and applications. *Annu. Rev. Control.* **2005**, *29*, 71–85. [CrossRef]
32. Hwang, I.; Kim, S.; Kim, Y.; Seah, C.E. A Survey of Fault Detection, Isolation, and Reconfiguration Methods. *IEEE Trans. Control. Syst. Technol.* **2010**, *18*, 636–653. [CrossRef]
33. Alavi, M.; Luo, M.; Wang, D.; Zhang, D. Fault diagnosis for power electronic inverters: A model-based approach. In Proceedings of the 8th IEEE Symposium on Diagnostics for Electrical Machines, Power Electronics & Drives, Bologna, Italy, 5–8 September 2011; pp. 221–228. [CrossRef]
34. Kou, L.; Liu, C.; Cai, G.W.; Zhang, Z. Fault Diagnosis for Power Electronics Converters based on Deep Feedforward Network and Wavelet Compression. *Electr. Power Syst. Research* **2020**, *185*, 106370. [CrossRef]
35. Box, G.E.; Jenkins, G.M.; Reinsel, G.C.; Ljung, G.M. *Time Series Analysis: Forecasting and Control*; John Wiley & Sons: Hoboken, NJ, USA, 2015.
36. Kay, S.M. *Modern Spectral Estimation*; Prentice Hall: Upper Saddle River, NJ, USA, 1988.
37. Stoica, P.; Moses, R.L. *Spectral Analysis of Signals*; Pearson Prentice Hall Upper: Saddle River, NJ, USA, 2005.
38. Baillie, D.; Mathew, J. A comparison of autoregressive modeling techniques for fault diagnosis of rolling element bearings. *Mech. Syst. Signal Process.* **1996**, *10*, 1–17. [CrossRef]
39. Wang, W.; Wong, A.K. Autoregressive model-based gear fault diagnosis. *J. Vib. Acoust.* **2002**, *124*, 172–179. [CrossRef]
40. Stack, J.; Habetler, T.; Harley, R. Bearing fault detection via autoregressive stator current modeling. *IEEE Trans. Ind. Appl.* **2004**, *40*, 740–747. [CrossRef]
41. Isermann, R. *Fault-Diagnosis Systems: An Introduction from Fault Detection to Fault Tolerance*; Springer Science & Business Media: Berlin/Heidelberg, Germany, 2006.
42. Junsheng, C.; Dejie, Y.; Yu, Y. A fault diagnosis approach for roller bearings based on EMD method and AR model. *Mech. Syst. Signal Process.* **2006**, *20*, 350–362. [CrossRef]
43. Barbieri, M.; Diversi, R.; Tilli, A. Condition monitoring of ball bearings using estimated AR models as logistic regression features. In Proceedings of the 2019 18th European Control Conference (ECC), Naples, Italy, 25–28 June 2019; pp. 3904–3909. [CrossRef]
44. Diversi, R.; Speciale, N.; Barbieri, M. Combining wavelets and AR identification for condition monitoring of electric-cam mechanisms using PLCopen readings of motor torque. *Int. J. Progn. Health Manag.* **2024**, *15*, 1–16. [CrossRef]
45. Barbieri, M.; Bosso, A.; Conficoni, C.; Diversi, R.; Sartini, M.; Tilli, A. An Onboard Model-of-signals Approach for Condition Monitoring in Automatic Machines. In *Enterprise Interoperability*; John Wiley & Sons, Ltd.: Hoboken, NJ, USA, 2018; Chapter 32, pp. 263–269. [CrossRef]
46. Barbieri, M.; Nguyen, K.T.; Diversi, R.; Medjaher, K.; Tilli, A. RUL prediction for automatic machines: A mixed edge-cloud solution based on model-of-signals and particle filtering techniques. *J. Intell. Manuf.* **2021**, *32*, 1421–1440. [CrossRef]
47. Lee, J.; Wu, F.; Zhao, W.; Ghaffari, M.; Liao, L.; Siegel, D. Prognostics and health management design for rotary machinery systems—Reviews, methodology and applications. *Mech. Syst. Signal Process.* **2014**, *42*, 314–334. [CrossRef]
48. Atamuradov, V.; Medjaher, K.; Dersin, P.; Lamoureux, B.; Zerhouni, N. Prognostics and health management for maintenance practitioners - Review, implementation and tools evaluation. *Int. J. Progn. Health Manag.* **2017**, *8*, 1–31. [CrossRef]
49. Soualhi, A.; Lamraoui, M.; Elyousfi, B.; Razik, H. PHM SURVEY: Implementation of Prognostic Methods for Monitoring Industrial Systems. *Energies* **2022**, *15*, 6909. [CrossRef]
50. Ott, H.W. *Electromagnetic Compatibility Engineering*; John Wiley & Sons: Hoboken, NJ, USA, 2011.
51. Mariscotti, A. Analysis of the DC-link current spectrum in voltage source inverters. *IEEE Trans. Circuits Syst. Fundam. Theory Appl.* **2002**, *49*, 484–491. [CrossRef]
52. Cox, S.M. Voltage and current spectra for a single-phase voltage source inverter. *IMA J. Appl. Math.* **2009**, *74*, 782–805. [CrossRef]
53. Pei, X.; Zhou, W.; Kang, Y. Analysis and Calculation of DC-Link Current and Voltage Ripples for Three-Phase Inverter with Unbalanced Load. *IEEE Trans. Power Electron.* **2015**, *30*, 5401–5412. [CrossRef]
54. Abari, I.; Lahouar, A.; Hamouda, M.; Slama, J.B.H.; Al-Haddad, K. Fault Detection Methods for Three-Level NPC Inverter Based on DC-Bus Electromagnetic Signatures. *IEEE Trans. Ind. Electron.* **2018**, *65*, 5224–5236. [CrossRef]

55. Linear Technology Corporation. LT Spice XVII (x64), Ver. 17.0.37.0. 2024. Available online: https://www.analog.com/en/resources/design-tools-and-calculators/ltspice-simulator.html (accessed on 24 July 2024).

56. Basseville, M. Distance measures for signal processing and pattern recognition. *Signal Process.* **1989**, *18*, 349–369. [CrossRef]

57. Mechefske, C.; Mathew, J. Fault detection and diagnosis in low speed rolling element bearings Part II: The use of nearest neighbour classification. *Mech. Syst. Signal Process.* **1992**, *6*, 309–316. [CrossRef]

58. Dron, J.; Rasolofondraibe, L.; Bolaers, F.; Pavan, A. High-resolution methods in vibratory analysis: Application to ball bearing monitoring and production machine. *Int. J. Solids Struct.* **2001**, *38*, 4293–4313. [CrossRef]

59. He, Q.; Du, D.; Wang, X. Autoregressive Model-Based Vibration Fault Diagnosis of Rolling Bearing. *Noise Vib. Worldw.* **2010**, *41*, 22–28. [CrossRef]

60. Nikhar, N.K.; Patankar, S.S.; Kulkarni, J.V. Gear tooth fault detection by autoregressive modelling. In Proceedings of the 2013 Fourth International Conference on Computing, Communications and Networking Technologies (ICCCNT), Tiruchengode, India, 4–6 July 2013; pp. 1–6. [CrossRef]

61. Quirk, M.; Liu, B. Improving resolution for autoregressive spectral estimation by decimation. *IEEE Trans. Acoust. Speech Signal Process.* **1983**, *31*, 630–637. [CrossRef]